



HAL
open science

Influence of the solar wind dynamic pressure on the ion precipitation: MAVEN observations and simulation results

Antoine Martinez, Ronan Modolo, François Leblanc, Jean-Yves Chaufray, Olivier Witasse, N. Romanelli, Y. Dong, T. Hara, J. Halekas, R. Lillis, et al.

► To cite this version:

Antoine Martinez, Ronan Modolo, François Leblanc, Jean-Yves Chaufray, Olivier Witasse, et al.. Influence of the solar wind dynamic pressure on the ion precipitation: MAVEN observations and simulation results. *Journal of Geophysical Research Space Physics*, 2020, 125 (10), pp.e2020JA028183. 10.1029/2020JA028183 . insu-02950993

HAL Id: insu-02950993

<https://insu.hal.science/insu-02950993>

Submitted on 16 Dec 2020

HAL is a multi-disciplinary open access archive for the deposit and dissemination of scientific research documents, whether they are published or not. The documents may come from teaching and research institutions in France or abroad, or from public or private research centers.

L'archive ouverte pluridisciplinaire **HAL**, est destinée au dépôt et à la diffusion de documents scientifiques de niveau recherche, publiés ou non, émanant des établissements d'enseignement et de recherche français ou étrangers, des laboratoires publics ou privés.

Influence of the solar wind dynamic pressure on the ion precipitation: MAVEN observations and simulation results.

A. Martinez¹, R. Modolo², F. Leblanc¹, J. Y. Chaufray^{1,2}, O. Witasse³, N. Romanelli⁴, Y. Dong⁵, T. Hara⁶, J. Halekas⁷, R. Lillis⁶, J. McFadden⁶, F. Eparvier⁷, L. Leclercq⁸, J. Luhmann⁶, S. Curry⁶ and B. Jakosky⁷.

¹ LATMOS/IPSL Sorbonne Université, UVSQ, CNRS, Paris, France

² LATMOS/IPSL, UVSQ Université Paris-Saclay, Sorbonne Université, CNRS, Guyancourt, France

³ ESTEC, European Space Agency, Noordwijk, Netherlands

⁴ Solar System Exploration Division, NASA Goddard Space Flight Center, Greenbelt, MD, USA. CRESST II, University of Maryland, Baltimore County, Baltimore, MD, USA.

⁵ Laboratory for Atmospheric and Space Physics, University of Colorado, Boulder, CO, USA

⁶ Space Science Laboratory, University of California, Berkeley, CA, USA

⁷ Department of Physics and Astronomy, University of Iowa, IA, USA

⁸ University of Virginia, Charlottesville, VA 22904, USA.

17 **Abstract:**

18 Using the data from the SWIA and STATIC instruments on board Mars Atmosphere and Volatile
19 Evolution (MAVEN) and LatHyS (Latmos Hybrid Simulation) simulations, we investigate the heavy ion
20 precipitation into the Martian atmosphere. We discuss the influence of the solar wind dynamic
21 pressure on the ion precipitation using observations performed by MAVEN from 04 June 2014 to 20
22 July 2017. The increase of the dynamic pressure from 0.63 to 1.44nPa is clearly associated with an
23 increase of the same order of magnitude of the precipitating oxygen ion energy flux measured by
24 MAVEN/STATIC from 9.9 to $20.6 \times 10^6 \text{eV} \cdot \text{cm}^{-2} \cdot \text{sr}^{-1} \cdot \text{s}^{-1}$ at low energy (from 30 to 650 eV). In the
25 same way, from 650 eV to 25000 eV, MAVEN/SWIA (all species) observed an increase from 22.4 to
26 $42.8 \times 10^7 \text{eV} \cdot \text{cm}^{-2} \cdot \text{sr}^{-1} \cdot \text{s}^{-1}$ of the precipitating ion energy flux.

27 Performing two simulations using the average solar wind conditions for both solar dynamic pressure
28 regimes observed by MAVEN as input in the LatHyS model, we reproduce some of the key
29 characteristics of the observed oxygen ion precipitation. We characterize the oxygen ions simulated
30 by LatHyS by their energy and time of impact, their time of injection in the simulation and initial
31 position and the mechanism by which these ions were created. The model suggests that the main
32 cause of the increase of the heavy ion precipitation during an increase of the solar dynamic pressure
33 is the increase of the ion production by charge exchange, proportional to the increase of the solar wind
34 flux, which becomes the main contribution to the ion precipitation at high energy.

35

36

37 I. Introduction

38

39 In the absence of a global magnetic field, Mars' upper atmosphere interacts directly with the solar
40 wind. Planetary neutral species (mainly carbon dioxide molecules, hydrogen and oxygen atoms) are
41 ionized by photoionization, electronic impact or charge exchange and are accelerated by the motional
42 electric field of the solar wind. These charged particles can precipitate into Mars' atmosphere with
43 energy up to several keV and induce a cascade of collisions, transferring enough energy to atmospheric
44 particles to exceed the Martian escape velocity (Luhmann and Kozyra, 1991; Johnson, 1994). While
45 this process, named atmospheric sputtering, may have led to significant atmospheric escape in its early
46 history, as suggested by Luhmann et al. (1992), its contribution is nowadays minor compared to other
47 neutral escape processes like Jeans escape (Anderson and Hord, 1971; Krasnopolsky and Feldman,
48 2001) and photochemical escape (Lillis et al., 2015; 2017), or ion escape process like pick-up ions
49 (Luhmann, 1990; Fang et al., 2010; Dong et al., 2017) and ion outflow (Lundin et al., 1990; Andersson
50 et al., 2010).

51 Atmospheric escape induced by sputtering at the present epoch is expected to be small compared to
52 other mechanisms (Leblanc et al. 2017) and therefore difficult to quantify from direct measurements.
53 However, since heavy planetary ion precipitation (which we define as having mass larger or equal to
54 the mass of carbon atom) is the primary driver of atmospheric sputtering (Johnson et al, 2000; Wang
55 et al, 2014; 2015), it is essential to constrain the dependence of the precipitating ion flux on present
56 solar wind conditions in order to, potentially, extrapolate the effect of this mechanism, over the
57 Martian history. In situ measurements of precipitating ions began with Mars Express (MEX) spacecraft,
58 in orbit around Mars since December 2003, (e.g., Chicarro et al., 2004; Barabash et al., 2006). Hara et
59 al. (2011) reported that MEX observed enhancements of precipitating heavy ions (e.g. O^+ and O_2^+)
60 during the passage of Corotating Interaction Region (CIR) solar wind structures. This observation
61 suggests that heavy ion precipitation is highly variable and depends on the upstream solar wind

62 conditions at Mars. Thanks to Mars Atmosphere and Volatile Evolution (MAVEN) measurements,
63 observations of heavy ion precipitation during quiet solar wind conditions have been reported by
64 Leblanc et al. (2015), suggesting that atmospheric sputtering occurs almost continuously at Mars.

65 Several investigations, either from observational or modeling studies, have highlighted the influence
66 of the plasma properties on the Martian environment. Edberg et al. (2009), Hall et al. (2016), Halekas
67 et al. (2017) and Ramstad et al. (2017) have shown that the solar EUV irradiance and the solar wind
68 dynamic pressure have an influence on the position of plasma boundaries such as the Magnetic Pile-
69 up Boundary (MPB) and the Bow Shock (BS). Indeed, the newly created exospheric ions can act to slow
70 the solar wind flux, which can move the bow shock position away from the planet (Hall et al, 2016).
71 Moreover, Lundin et al. (2008) also showed that the size of the Martian obstacle (estimated as
72 proportional to the BS position) influences the ion atmospheric escape rate.

73 The statistical study by Hara et al. (2017a) has showed that precipitating ion fluxes observed by MAVEN
74 (Jakosky et al., 2015) vary at least by an order of magnitude (typically between $10^4 \text{ cm}^{-2} \cdot \text{s}^{-1} \text{sr}^{-1}$ and
75 $10^6 \text{ cm}^{-2} \cdot \text{s}^{-1} \text{sr}^{-1}$ for ions with energies higher than 25 eV) depending on the upstream solar wind
76 conditions such as the dynamic pressure, the magnitude of the interplanetary magnetic field, and the
77 motional electric field direction $\vec{E} = -\vec{V}_{\text{SW}} \times \vec{B}_{\text{SW}}$ with \vec{V}_{SW} the solar wind velocity and \vec{B}_{SW} the
78 interplanetary magnetic field vector. Indeed, it has been shown by several theoretical studies
79 (Luhmann and Kozyra 1991; Chaufray et al. 2007; Curry et al. 2015) that the orientation of the motional
80 electric field may influence the energy and intensity of ion precipitation on Mars. These studies
81 suggested that the integrated total precipitating ion fluxes are globally larger in the $-\vec{E}$ hemisphere
82 than in the $+\vec{E}$ hemisphere. Pickup oxygen ions formed in the $-\vec{E}$ hemisphere are accelerated towards
83 Mars and can precipitate while oxygen ions formed in the $+\vec{E}$ hemisphere are accelerated away from
84 Mars and can escape. Such results have been observed by Martinez et al. (2019a) and Hara et al.
85 (2017a) thanks to MAVEN.

86 Curry et al. (2015) have studied the response of Mars O⁺ pickup ions to an ICME (March 8th, 2015) with
87 a test-particle approach and found that the oxygen ion precipitation depends on the phase of the ICME
88 with a maximum of precipitation during the shock. After the passage of the ICME shock, the
89 precipitating flux of the ejecta phase decreases but still remains greater than the precipitating flux
90 during the pre-ICME phase. Based on a similar approach, Fang et al. (2013) have shown that oxygen
91 ion precipitation can vary by at least one order of magnitude due to the variation in dynamic pressure
92 during ICME or CIR solar wind events. Similar conclusions have been reported by Hara et al. (2011)
93 with Mars Express observation or by Martinez et al. (2019a) with MAVEN observations during the
94 September 2017 solar events (Lee et al. 2018).

95 Complementary to observations, models can provide an extended set of information to better
96 characterize the physical processes under investigations. By being able to take into account a wide
97 variety of physical processes in time and space, models can be used to reproduce observations and
98 investigate the resulting mechanisms. They provide a three-dimensional context for the observations.
99 At the beginning of Martian exploration, with Mariner 4 or Phobos 2, computer simulations have been
100 found very useful for investigating the physic mechanisms of the atmospheric escape (Luhmann and
101 Kozyra, 1991; Luhmann, Jonhson & Zhang, 1992; Johnson, 1994; Leblanc & Johnson, 2001; 2002;
102 Dubinin & Lundin, 1995; Fang et al., 2010). Some studies also make it possible to model the present
103 and past contributions of these mechanisms to atmospheric escape (Chassefière & Leblanc, 2004).
104 Combining MEX observations and sophisticated global model simulations, Diéval et al. (2012) have
105 shown that the precipitating protons originate from both the solar wind and the planetary exosphere.
106 Here, we use model to simulate the potential effects of the solar dynamic pressure on the ion
107 precipitation.

108 In this paper, we further analyze the role of the solar dynamic pressure on the ion precipitation by
109 performing a detailed analysis of MAVEN measurements combined with the simulation of its potential
110 effects. The LATMOS Hybrid Simulation (LatHyS) model (Modolo et al, 2016) is used to constrain the
111 processes that may control the ion precipitation. The instruments and data used to perform this

112 analysis, as well as the methodology developed are described in section II. The model is described in
113 section III whereas section IV present the main results and lessons derived from the
114 simulation/measurement comparisons and section V the conclusions.

115

116 II. MAVEN measurements of the solar wind conditions and precipitating ion flux

117 A. Instruments and Data

118 The large set of MAVEN instruments (Jakosky et al. 2015) allows us to characterize the precipitating
119 ion flux as well as the upstream solar wind conditions and also to constrain the atmospheric and plasma
120 properties of the Martian environment. In this study, we use measurements performed by the Solar
121 Wind Ion Analyzer (SWIA; Halekas et al., 2015), the SupraThermal and Thermal Ion Composition
122 (STATIC; McFadden et al., 2015), the Magnetometer (MAG; Connerney et al., 2015a; 2015b) and the
123 Solar Extreme Ultraviolet Monitor (EUVM; Eparvier et al., 2015). The MAVEN/SWIA instrument is an
124 energy and angular ion spectrometer. In this work, we use the SWIA coarse survey data product,
125 covering an energy range between 25 eV/q and 25 keV/q with 48 energy steps logarithmically spaced,
126 a field of view (FOV) of $360^\circ \times 90^\circ$ with 64 angular bins and 4s time resolution. The MAVEN/STATIC
127 instrument is an energy, mass and angular ion spectrometer. We used the STATIC “D1” data product,
128 covering an energy range between 0.1 eV/q and 35 keV/q with 32 energy steps logarithmically spaced,
129 a field of view (FOV) of $360^\circ \times 90^\circ$ on 64 angular bins and 8 mass bins covering a mass range from 1
130 amu to 80 amu with a 4s time resolution.

131 We mainly based our study on MAVEN/SWIA despite the lack of mass resolution because
132 MAVEN/STATIC operates mostly in conic mode (McFadden et al. 2015) below 350 km in altitude
133 leading to a limited coverage for ions with energy larger than 650 eV. In the following, we use
134 MAVEN/STATIC to refine our analysis for energies below 650 eV. Moreover, in order to avoid any
135 potential bias in the measurement due to spacecraft charging, we only consider precipitating ions with
136 energies larger than 30 eV. Although MAVEN/SWIA does not have mass resolution, it can be used to
137 estimate the evolution of heavy ion precipitation for the high energy range. Pickup ions can be

138 accelerated by the motional electric field up to a maximum energy limit (Jarvinen and Kallio, 2014;
139 Rahmati et al., 2015) which is:

$$140 \quad E_{max}(M^+) = 4 * m_M * U_{SW}^2 * \sin^2(\theta_{UB}) = 4 * E_{SW} * \left(\frac{m_M}{m_p}\right) * \sin^2(\theta_{UB}) \quad (1)$$

141 Where M^+ is the species with a mass m_M and θ_{UB} is the angle between the solar wind velocity and the
142 interplanetary magnetic field, m_p is the proton mass and E_{SW} is the energy of the solar wind proton.
143 The maximum energy is 4 times that of the solar wind, that is, typically around four times 800 eV to 1
144 keV for nominal conditions for planetary protons and four times 2.4 keV to 4 keV for planetary helium
145 ions. Therefore, any ions precipitating with energy larger than few keV are most probably planetary
146 ions with masses larger than the proton and helium masses.

147 The MAVEN/EUVM measures the solar irradiance in three bands from the soft X-ray to the EUV range
148 (in three spectral bands 0.1-7 nm, 17-22 nm and 121-122 nm) with a temporal resolution of 1s. To
149 characterize the solar EUV irradiance, we use MAVEN/EUVM channel A which measures solar
150 irradiance between 17 and 22 nm.

151 The solar wind density, solar wind velocity, and Interplanetary Magnetic Field (IMF) vectors are
152 measured by MAVEN/SWIA and MAVEN/MAG and averaged on an orbit-by-orbit basis while MAVEN
153 is in the pristine solar wind (Halekas et al., 2017). In this work, we use the Mars Solar Electric (MSE)
154 coordinate system in which the X-axis points toward the Sun, the Z-axis is aligned with the solar wind
155 motional electric field and the Y-axis completes the right hand system (Fedorov et al., 2006).

156

157 **B. Upstream and planetary conditions**

158 To investigate the dependence of the precipitating ion flux with respect to the solar wind dynamic
159 pressure, we used the method developed by Dong et al. (2017) and Martinez et al. (2019b). In absence
160 of permanent solar wind monitoring, we assume that the averaged solar wind parameters, measured
161 by MAVEN when inside the solar wind, are constant during the whole orbit as explained in Martinez et

162 al. (2019b). Solar wind parameters on an orbit-by-orbit basis, when MAVEN was in the solar wind, are
 163 then used to determine the average solar wind parameters for a given set of measurements.
 164 We organize MAVEN data into two sets of measurements corresponding to two different solar wind
 165 dynamic pressure conditions: a low dynamic pressure case with values between 0.3 and 1.0 nPa and a
 166 high dynamic pressure case with values between 1.0 and 2.6 nPa. The IMF strength (B_{IMF}) is also
 167 imposed between 2.2 and 6.7 nT. The solar wind dynamic pressure is defined as $P_{dyn} = m_p n_{SW} V_{SW}^2$,
 168 where m_p is the mass of the proton, n_{SW} and V_{SW} the solar wind density and velocity. For both sets of
 169 measurements, we determine the mean solar wind conditions and calculate the norm of the solar wind
 170 motional electric field defined as $E = |\overrightarrow{V_{SW}} \times \overrightarrow{B_{IMF}}|$, the solar wind particle flux defined as $F_{SW} =$
 171 $n_{SW} V_{SW}$, the Alfvén Mach number defined as $M_A = \frac{V_{SW}}{V_A}$ (with the V_A the Alfvén speed), the magneto-
 172 sonic Mach number M_{MS} as defined in Edberg et al., (2010) and the MSE angle as defined in Martinez
 173 et al., (2019a). The MSE angle corresponds to the anticlockwise angle between the MAVEN's location
 174 in MSE coordinates during its measurements of the precipitating ion flux and the East MSE direction
 175 (MSE longitude equal to $+180^\circ$ and latitude equal to 0°).

176
 177 These parameters are displayed in Table 1. The last column of Table 1 presents the coverage
 178 distribution, as defined in Martinez et al, (2019b), showing the percentage of common distribution for
 179 a given parameter between the two dynamic pressure groups. Except for the solar wind density and
 180 flux, and obviously for the dynamic pressure, all solar wind properties show similar variations with
 181 about 70 %, or more, of the distribution of each of these parameters in common. In other words, the
 182 EUV irradiance, IMF intensity, Alfvén and magnetosonic Mach numbers, solar wind speed and MSE
 183 angle are similar during these two sets of measurements. The spatial coverage of the ion precipitation
 184 measurements, characterized by the MSE angle and the solar zenith angle, is also similar during these
 185 two sets of measurements.

186

187 The presence of crustal magnetic fields (Acuña et al., 1999; Connerney et al., 2005) can influence locally
 188 the precipitating ion flux, as shown by Hara et al. (2017b). In order to limit the potential influence of
 189 the crustal fields (Leblanc et al. 2017; Hara et al. 2017b), we also only consider measurements
 190 performed when the average magnetic field between 200 and 350 km was less than 60 nT. Moreover,
 191 to further limit the potential role of the crustal fields on the precipitation, we also consider only
 192 MAVEN measurements performed when the main crustal field region (centered at 180° GEO East
 193 longitude and -50° GEO latitude) was in the nightside, meaning when the subsolar point has a GEO
 194 longitude from -60° to 60°.

195

		High Pdyn [1.0,2.6] nPa	Low Pdyn [0.3,1.0] nPa	Common coverage (%)
EUV Flux ($mW \cdot m^{-2}$)	$\mu \pm \sigma$	0.22 ± 0.04	0.22 ± 0.03	85.5
	Q25	0.19	0.20	
	Q75	0.24	0.23	
Dynamic pressure (nPa)	$\mu \pm \sigma$	1.44 ± 0.41	0.63 ± 0.19	0.0
	Q25	1.13	0.46	
	Q75	1.63	0.79	
Solar Zenith Angle (°)	$\mu \pm \sigma$	96 ± 28	96 ± 28	89.7
	Q25	80	77	
	Q75	115	118	
Electric field ($mV \cdot m^{-1}$)	$\mu \pm \sigma$	1.44 ± 0.55	1.04 ± 0.45	68.6
	Q25	1.00	0.74	
	Q75	1.77	1.20	
IMF (nT)	$\mu \pm \sigma$	3.90 ± 1.12	3.23 ± 0.95	69.1
	Q25	2.92	2.50	
	Q75	4.52	3.60	
Speed ($km \cdot s^{-1}$)	$\mu \pm \sigma$	448 ± 80	423 ± 78	80.1
	Q25	376	370	
	Q75	495	467	
Density (cm^{-3})	$\mu \pm \sigma$	4.67 ± 1.93	2.25 ± 0.97	40.9
	Q25	3.28	1.49	
	Q75	5.69	2.78	
MSE angle(°)	$\mu \pm \sigma$	178 ± 110	203 ± 110	86.2
	Q25	94.7	153	

	Q75	263	322	
Alfven Mach number	$\mu \pm \sigma$	11.5 ± 3.0	9.1 ± 2.5	68.9
	Q25	9.3	7.3	
	Q75	13.1	10.8	
Magnetosonic Mach number	$\mu \pm \sigma$	7.76 ± 1.36	7.10 ± 1.38	86.4
	Q25	6.83	6.10	
	Q75	8.58	8.07	
Solar wind flux ($10^8 \text{ cm}^{-2}\text{s}^{-1}$)	$\mu \pm \sigma$	1.98 ± 0.62	0.91 ± 0.29	23.5
	Q25	1.57	0.68	
	Q75	2.36	1.09	

196 **Table 1:** Mean μ , standard deviation σ , first quartile Q25 and third quartile Q75 of the solar zenith
197 angle and each solar planetary parameter distribution for the two sets of precipitating flux
198 measurement. The last column provides the percentage of the area in common between the two
199 distributions.

200

201 **C. MAVEN's ion precipitation measurements**

202 In order to reconstruct the precipitating ion energy flux, we use the method developed by Leblanc et
203 al. (2015) and Martinez et al (2019a). We use MAVEN observations of the two sets of measurements
204 performed between 200 and 350 km. Within such altitude range, any ions moving toward the planet
205 in a cone of less than 75° with respect to the local nadir direction has a very large probability to impact
206 Mars' atmosphere. Therefore, to reconstruct the precipitating flux, we sum all measurements of SWIA
207 (and STATIC) anodes with a FOV corresponding to a cone of less than 75° from the local zenith
208 direction. Moreover, in order to exclude the reconstructed precipitating flux with poor coverage, we
209 only consider measurements during which the total FOV of SWIA (and STATIC) anodes covers more
210 than 65 % of the 75° solid angle cone centered on the zenith direction. In the case of MAVEN/SWIA
211 measurements, which has a low signal-to-noise ratio at high energy, we adapted the method from
212 Martinez et al. (2019a) to remove an average background induced by Solar Energetic Particles (SEP).

213 Compared to MAVEN/SWIA, MAVEN/STATIC is less sensitive to SEPs because its measurements
214 technique is based on double coincidence (McFadden et al., 2015). In case of intense SEP events or
215 background level, STATIC measurements with poor quality were flagged and systematically excluded
216 from our analysis. So, the background level of MAVEN/STATIC is assumed to be negligible.

217

218 In this study, MAVEN observations obtained from June 4th, 2015 to July 20th, 2017 have been
219 categorized into two groups with similar spatial coverage: high dynamic pressure with 1.44 nPa
220 averaged on 226 ion precipitation spectra by MAVEN/SWIA, and low dynamic pressure with 0.63 nPa
221 averaged on 454 ion precipitation spectra by MAVEN/SWIA.

222

223 III. LatHyS Model

224

225 In order to simulate the Martian environment and the precipitating heavy ion flux, we choose to use
226 the hybrid approach which describes ions with a kinetic approach while the electrons are treated as a
227 fluid (Modolo et al. 2016). The hybrid model called LatHyS is a 3-D multispecies parallelized model that
228 simulates the interaction of the solar wind plasma with the neutral environment of the planet,
229 characterizing all plasma regions in the vicinity of the planet. A detailed description of the LatHyS
230 model can be found in Modolo et al. (2005 and 2016). The model uses as inputs a 3-D density
231 description of H, O and CO₂ representing the thermosphere and exosphere. The neutral species
232 description is modeled from the LMD - Global Circulation Model (Forget et al, 1999; Chaufray et al.
233 2014) and the Exospheric Global Model (Yagi et al, 2012; Leblanc et al, 2017). The state of the neutral
234 environment corresponds to solar longitude Ls = 270°. The spatial resolution of the LatHyS results
235 presented in this paper is $\Delta x = 57$ km, and a mean solar activity is assumed for all the models (LatHyS,
236 EGM, LMD-GCM) and for the two solar wind dynamic pressure cases.

237

238 Simulations are set up with typical solar wind parameters based on the orbit-by-orbit average solar
239 wind parameters for the two groups of solar wind dynamic pressure, from Table 1. To facilitate the
240 interpretation of the simulated precipitation fluxes, the interplanetary magnetic field is taken with only
241 a B_y component. For the period of high dynamic pressure we have: $n_{SW} = 4.7 \text{ cm}^{-3}$, $V_{SW} =$
242 450 km.s^{-1} and $B_y = 4.0 \text{ nT}$. For the period of low dynamic pressure we have: $n_{SW} = 2.2 \text{ cm}^{-3}$,
243 $V_{SW} = 424 \text{ km.s}^{-1}$ and $B_y = 3.2 \text{ nT}$. Simulations are performed with a sub-solar longitude at 0°
244 and a subsolar latitude at -23° , meaning that the main crustal field region is located in the nightside.
245 To further analyze simulation results, for each particle we record the information of the injection
246 position, the ionization mechanism of the particle, the injection time, the precipitation time and its
247 precipitating energy. Three main sources of ions are implemented in the simulation model. A simplified
248 set of ionospheric chemistry equations is included (below 350 km) and particles created in this region
249 are labeled as ionospheric particles. Particles can also be produced by photo-ionization above 350 km,
250 where the optical depth is negligible, or undergo charge exchange reactions. Information concerning
251 the ionization processes are detailed in Modolo et al. (2016).

252

253 In this study, we consider only oxygen ions. Heavier ions (such as Ar^+ , O_2^+ and CO_2^+) are not considered
254 because of their much lower density at high altitude according to Fox (2004) so that their contribution
255 to atmospheric sputtering should be very limited in intensity. Once a steady state of the simulation is
256 achieved, O^+ ion precipitating ($V_r < 0$) below 250 km in altitude are recorded in order to construct an
257 energy flux map on a $4.5^\circ \times 4.5^\circ$ longitude-by-latitude grid. To have meaningful statistics on the
258 precipitating O^+ ions, the accumulation is performed over 100 solar wind proton gyro-periods (about
259 6-7 transit times of the simulation box). Each energy spectra corresponding to the impacting O^+ flux is
260 computed with an energy resolution of $\frac{dE}{E} = \sim 17\%$ for energy larger than 2 eV. With more than one
261 million precipitating numerical particles for each simulation, the modelled sample is large enough to
262 be statistically significant. The stationarity of the solution has been checked by comparing energy

263 spectra at each grid point of the map for various accumulation intervals. We found a temporal standard
264 deviation of 15-20 % indicating that the simulation converged to a stable solution.

265

266 In order to compare simulation and observation, a similar methodology to reconstruct the simulated
267 precipitation as for MAVEN measurements have been used:

268 - For each sequence of observation, the portion of MAVEN trajectory during which the
269 precipitating flux was measured (between 200 km and 350 km in altitude) is
270 reconstructed in the simulated MSE reference frame.

271 - The simulated energy spectra of the precipitating flux along each of these portions of
272 MAVEN trajectory are then reconstructed and averaged. If, for a given energy bin, the
273 simulated flux is lower than the threshold corresponding to MAVEN/SWIA background,
274 the simulated precipitated ion energy flux, for this energy bin, is not considered to
275 calculate the average.

276

277 IV. LatHyS simulated precipitation and MAVEN precipitating measurements

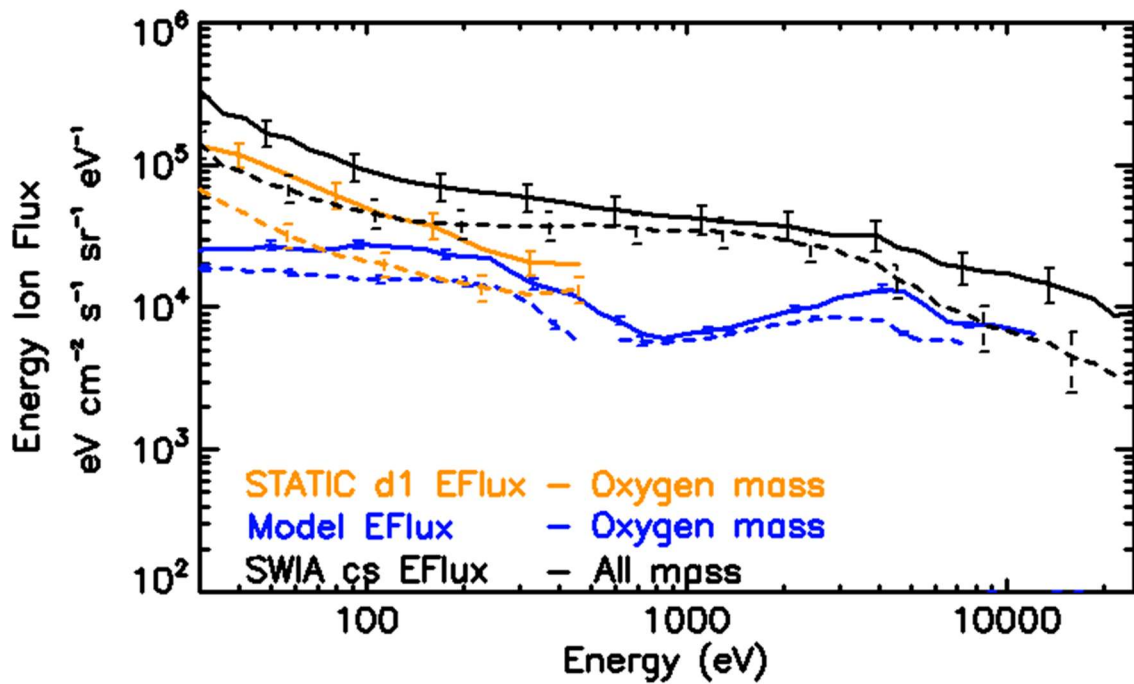
278 A. Comparison between MAVEN observation of the precipitating flux and LatHyS simulated 279 flux

280 Figure 1 shows the comparison of the spectrum of the average precipitating ion energy flux for
281 MAVEN/SWIA, MAVEN/STATIC and as simulated for the two dynamic pressure cases. The energy
282 dependence of the differential flux is similar from one solar wind dynamic pressure case to the other
283 for both instruments. For both dynamic pressure cases, the low-energy component of the precipitating
284 oxygen ion energy flux measured by MAVEN/STATIC and simulated follow similar dependency with
285 higher fluxes for larger dynamic pressure. Below 50 eV, we notice an increasing discrepancy between
286 observation and simulation. This difference can be, in part, explained by the limited resolution of the
287 simulations (57 km). At low energy, the main component of the oxygen ion precipitation comes from
288 the ionospheric region (below 350 km in altitude) where the spatial resolution of the simulation

289 remains several times higher than the thermospheric height scale (11-20 km). Because of this, ion
290 production in the ionosphere (below 350 km in altitude) is probably poorly described, making it less
291 sensitive to any external variations.

292 For energy larger than a few keVs, as explained in section II.A, MAVEN/SWIA observed ion precipitation
293 should be in large proportion composed of O⁺ ions. Above 3 to 4 keV, there is a clear increase of the
294 measured and simulated precipitating fluxes from the low dynamic pressure case to the high dynamic
295 pressure case. The gap between the MAVEN/SWIA curves (all species) and those of the model (only
296 oxygen ions) between 300 eV and 3-4keV can be explained by the contribution of other species in the
297 observed ion precipitation (mainly protons, in particular around the solar wind energy, probably
298 produced in the hydrogen corona).

299 Table 2 shows the integrated precipitating ion energy flux for each dynamic pressure case and two
300 energy ranges: low energy [30-650] eV) and high energy [650-25000] eV. The ion precipitation
301 increases when the dynamic pressure of the solar wind increases, as previously observed by Hara et
302 al. (2017a) with MAVEN/SWIA and MAVEN/STATIC measurements. It increases by a factor between
303 1.7 and 2.0 at low energy and by factor 1.9 to 2.1 at high energy. Both simulation and observation
304 agree relatively well when comparing the two dynamic pressure cases, even if the simulation predicts
305 a systematic factor ~4 lower integrated flux with respect to SWIA observed precipitation for both solar
306 dynamic pressure cases and energy ranges. At high energy, this factor can be partially explained by the
307 fact that the modelled precipitating ion energy flux becomes lower than the MAVEN/SWIA background
308 and so, the energy ion flux is not considerate, which slightly underestimate the modelled ion
309 precipitation. In other words, even if the simulation did not perfectly reproduce the absolute intensity
310 of the observed precipitation, the simulated variation of the precipitating flux with increasing pressure
311 might be driven by a similar mechanism to the one controlling the dependency of this flux in MAVEN
312 observations.



313

314

Figure 1: Average precipitating ion differential energy spectra as measured by MAVEN/SWIA

315

(black – all species), MAVEN/STATIC (orange – oxygen mass) and simulated (blue – oxygen mass)

316

during high pressure period (line) and low pressure period (dashed line). The vertical lines

317

correspond to the standard error of the average flux.

318

		Integrated precipitating ion energy flux	
		Low energy [30-650] eV	High energy [650-25000] eV
High pressure period	SWIA (all species)	$4.27 (\pm 0.93) \times 10^7$	$42.8 (\pm 11.1) \times 10^7$
	STATIC	$2.06 (\pm 0.41) \times 10^7$	XXXXXXXXXX
	Model	$1.03 (\pm 0.08) \times 10^7$	$10.8 (\pm 0.6) \times 10^7$
	SWIA	$2.57 (\pm 0.58) \times 10^7$	$22.4 (\pm 7.2) \times 10^7$

Low pressure period	(all species)		
	STATIC	$9.89 (\pm 1.98) \times 10^6$	
	Model	$6.07 (\pm 0.04) \times 10^6$	$5.10 (\pm 0.15) \times 10^7$
Ratio HPDYN/LPDYN	SWIA (all species)	1.66	1.91
	STATIC	2.08	
	Model	1.70	2.12

319 **Table 2:** Integrated precipitating ion energy flux as measured by MAVEN/STATIC (only oxygen ion)
320 and MAVEN/SWIA (all species) and modelled by LatHyS (only oxygen ion) for each period. The last
321 three line correspond to the ratio between the high pressure period values and the low pressure
322 period values for each instrument. In brackets, the 1-sigma standard deviation (uncertainty) of the
323 precipitating ion energy flux values. The integrated ion precipitation unit is in $eV \cdot cm^{-2} \cdot sr^{-1} \cdot s^{-1}$.

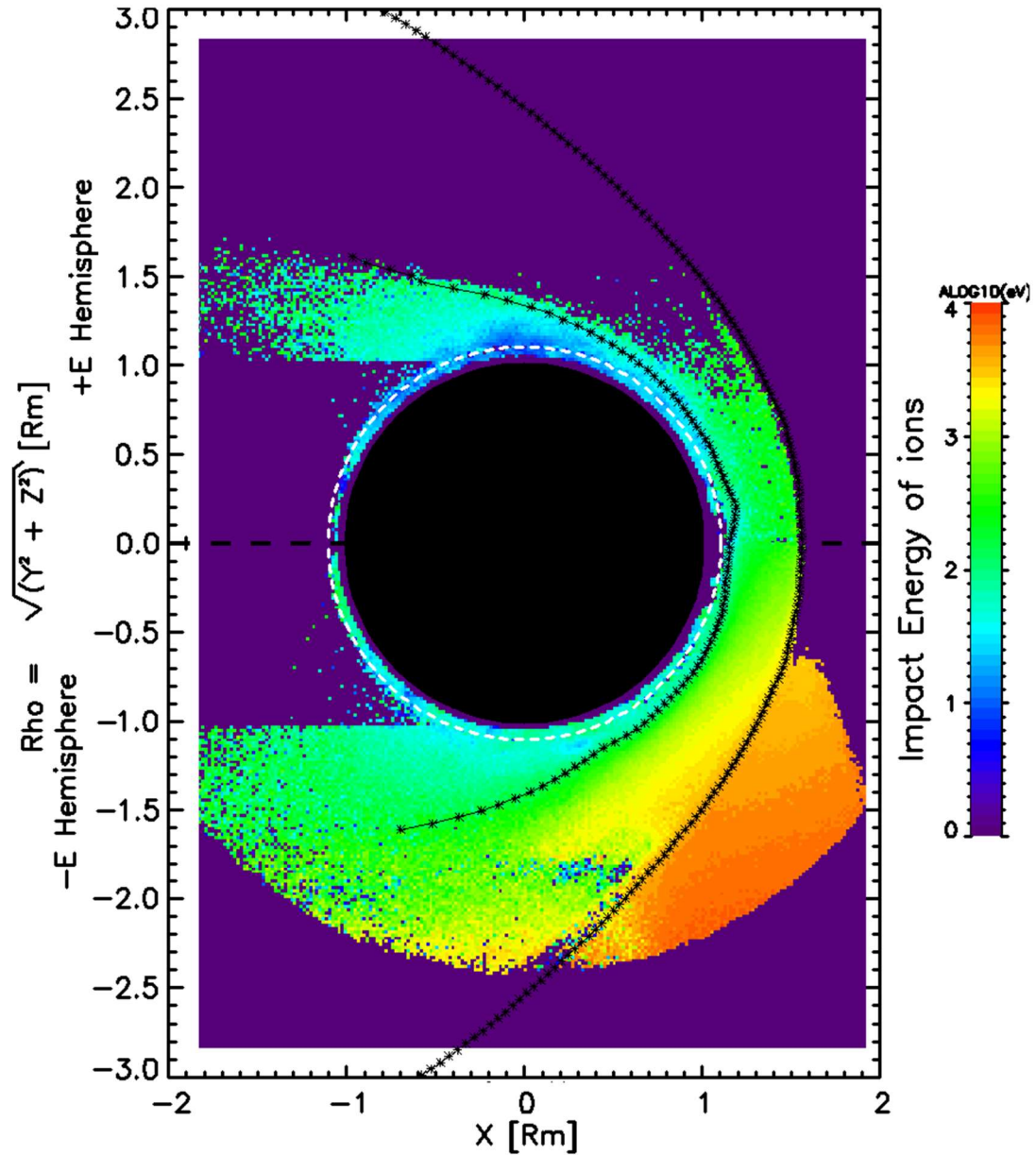
324

325 B. Origins and parameters controlling the simulated precipitating fluxes

326 Figure 2 displays the impact energy of the precipitating oxygen ions (of ionospheric origin, created by
327 photo-ionization or by charge exchange) as a function of their injection (creation) position in the (X, ρ)
328 coordinate system with $\rho = \sqrt{Y^2 + Z^2}$, for the low pressure case. The negative values of ρ
329 correspond to the Southern Hemisphere MSE ($Z < 0$) while positive values indicate the Northern
330 Hemisphere ($Z > 0$). The lack of injected particles behind Mars is explained by the shadow of the planet,
331 preventing photo-ionizations. The precipitating ions with energy higher than the solar wind (800 eV -
332 1 keV) are formed in the southern hemisphere MSE and their final energy depends on their altitude of
333 creation (by ionization). This energy-altitude injection relation is consistent with Jarvinen et al. (2018)
334 and can be explained by the time spent by an ion in the high electric field regions (essentially the solar
335 wind and the magnetosheath). In the northern hemisphere, it can also be seen that precipitating ions
336 are mainly formed within or downstream of the pile-up magnetic region. The high-energy ions

337 precipitate mainly in the Southern hemisphere and on the Martian dayside (not shown) as simulated
338 in Luhmann and Kozyra (1991). This distribution of the origin position of precipitating ions and their
339 impact energy can be explained by the intensity of the electric field and its direction (Chaufray et al.,
340 2007; Curry et al., 2015). In the upstream solar wind and the magnetosheath, the newly born ions will
341 be accelerated in the direction of the convective electric field. Ions formed in the northern hemisphere
342 MSE will be moved away Mars, while ions formed in the southern hemisphere MSE will be accelerated
343 toward Mars, as observed in Hara et al. (2017a). This is why for high $X > 0$ and $\rho > -0.5$ in Figure 2,
344 there are almost no precipitating ions formed upstream the bow shock. The ions formed inside the
345 magnetosheath will see a disturbed electric field direction which may lead them to precipitate. To
346 summarize, this result indicates that oxygen ions created above the ionosphere in the $-E$ hemisphere
347 can more easily precipitate toward the planet rather than those created in the $+E$ hemisphere, in good
348 agreement with previous numerical simulations (Chaufray et al., 2007; Fang et al., 2010; Curry et al.,
349 2015).

350



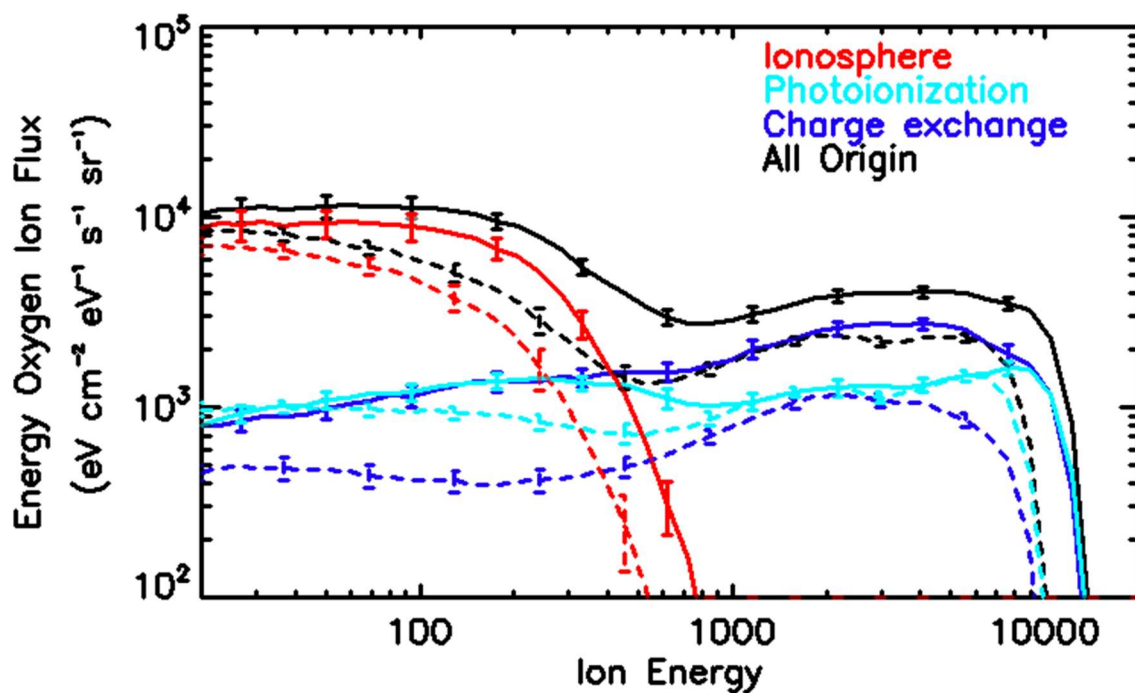
351

352 Figure 2: Map of the origin position of the precipitating ions produced either in the ionosphere (below
 353 350 km in altitude), by photo-ionization or by charge exchange for the low pressure period. The impact
 354 energy of the modelled ions is shown in color. The black lines correspond to the ion magnetopause
 355 boundary (closest to Mars) and bow shock (farthest from Mars) location. The dashed white circle
 356 corresponds to the upper limit of the ionosphere (350 km in altitude).

357

358 Figure 3 displays the energy distribution of the simulated precipitating oxygen ion energy flux averaged
 359 over the whole oxygen ion precipitation map (without removing the background value of
 360 MAVEN/SWIA). In the high dynamic pressure case, the maximum energy of the ions impacting the
 361 atmosphere reaches 14 keV whereas in the low dynamic pressure case only 10 keV. This illustrates the
 362 fact that ions created at the same position see a stronger electric field intensity in the case of high
 363 pressure ($E = 1.44 \text{ mV} \cdot \text{m}^{-1}$ upstream of the bow shock) than in the case of the low pressure ($E =$
 364 $1.04 \text{ mV} \cdot \text{m}^{-1}$ upstream of the bow shock)

365 As a matter of fact, the main difference between the two modelled dynamic pressure cases can be
 366 described as a global shift in energy, associated with a change in the local electric field intensity, and
 367 an increase of the intensity of the precipitating ions. As an example, in the case of the ionospheric ions
 368 (red lines in Figure 3), there is a significant increase of the precipitating flux with increasing dynamic
 369 pressure above 50 eV, as observed by the MAVEN/STATIC. In the same way, in the case of the ions
 370 produced by photoionization Figure 3, there is globally an increase in energy of the precipitating ions
 371 due to the increase of the electric field close to Mars when increasing the dynamic pressure.



372

373 Figure 3: Simulated precipitating oxygen ion differential energy spectra. Solid line: high dynamic
374 pressure case. Dashed line: low dynamic pressure case. Red lines: oxygen ionospheric ions. Dark blue
375 lines: oxygen ions produced by charge exchange. Light blue lines: oxygen ions produced by photo-
376 ionization. Black lines: total precipitating oxygen ions flux. Vertical lines: standard deviation of the flux
377 estimated by performing several snapshots during the simulation.

378

379 However, in the case of the ion produced by charge exchange, a higher dynamic pressure induces not
380 only a gain of energy of the precipitating particle but also an increase in the charge exchange ionization
381 rate between solar wind protons and O atmospheric neutral particles which should be proportional to
382 the solar wind particle flux $\sim n_{SW}V_{SW}$. The ionization rate by charge exchange should increase by a
383 factor ~ 2.3 which is the ratio between the solar wind flux in the high dynamic pressure case to the
384 solar wind flux in the low dynamic pressure case. This ratio is very close to the ratio of the precipitating
385 fluxes of the ions produced by charge exchange between the high and low dynamic pressure cases
386 (equal to ~ 2.7). On the other hand, the production rates of ion in the ionosphere or by photo-ionization
387 are not or only in a limited way influenced by the change of the solar wind dynamic pressure. As shown
388 in Figure 3 in the case of the high dynamic pressure (dark blue line), the precipitating flux is dominated
389 by ions produced by charge exchange above 1 keV. In the low dynamic pressure case, charge exchange
390 and photo-ionization produces roughly the same amount of ions according to the simulation.

391 The main lessons from the simulation are:

- 392
- 393 - An increase of the dynamic pressure should lead to a global increase of the energy of
394 the ion precipitating in the atmosphere, roughly proportionally with the change of the
395 motional electric field in the undisturbed solar wind.
 - 396 - An increase of the dynamic pressure should lead to an increase of the charge exchange
397 rate in a proportion roughly equivalent to the increase in solar wind flux. This effect
should be observable at high energy, above typically 1 keV, where the contribution of

398 the charge exchange mechanism on the production of the precipitating ion starts to
399 dominate.
400 - Below 1 keV, the precipitating ion energy flux should be dominated by the ionospheric
401 ions which are poorly described by LatHyS due to a limitation in spatial resolution.

402 We also evaluated the impact of the dynamic pressure on the plasma boundaries (essentially on the
403 bow shock position) by comparing the precipitating flux of oxygen ions produced by photo-ionization
404 upstream of the bow shock for both cases. With a small difference between the two cases, we
405 concluded that the precipitating ion flux is only weakly influenced by the compression of the bow shock
406 with increasing solar dynamic pressure (see supplementary document).

407

408 V. Summary and Conclusion

409 Solar wind observations around Mars from the MAVEN spacecraft from 04 June 2015 to 20 July 2017
410 are organized into two sets of measurements corresponding to two periods of significantly different
411 solar dynamic pressure. Beside different solar wind conditions, all other parameters that could
412 potentially influence the state of Mars' atmosphere and magnetosphere are carefully estimated in
413 order to be equivalent in both samples (by selecting only observations with the same solar conditions
414 and geographic coverage). From these two periods, we then use MAVEN portions of orbit between
415 350 and 200 km in altitude to reconstruct the precipitating ion energy fluxes from SWIA (Halekas et al.
416 2015) and STATIC (McFadden et al. 2015) measurements following the method developed in Leblanc
417 et al. (2015) and Martinez et al. (2019a).

418 The average solar conditions of each period are then used to simulate Mars' environment using LatHyS
419 hybrid model (Modolo et al. 2016). These two simulations are realized for the same solar extreme
420 ultra-violet conditions, the same season of the Martian atmosphere (LS = 270°), with the same
421 orientation of the Interplanetary Magnetic Field and the main crustal field placed in the nightside. A

422 method is also developed in order to reconstruct the oxygen ion precipitation from both simulations
423 using the same approach as when analyzing MAVEN measurements.

424 The precipitating ion energy flux measured by MAVEN/STATIC and MAVEN/SWIA increases with the
425 increase of the solar wind dynamic pressure, which is consistent with previous studies (Hara et al.,
426 2017a). The increase of the dynamic pressure from 0.63 to 1.44 nPa is clearly associated with an
427 increase at the same order of the precipitating oxygen ion energy flux measured by MAVEN/STATIC
428 from 9.9 to $20.6 \times 10^6 \text{ eV} \cdot \text{cm}^{-2} \cdot \text{sr}^{-1} \cdot \text{s}^{-1}$ (a ratio of ~ 2.1) for the low energy range (from 30 to 650
429 eV). From 650 eV to 25000 eV, observations by MAVEN/SWIA show an increase from 22.4 to $42.8 \times$
430 $10^7 \text{ eV} \cdot \text{cm}^{-2} \cdot \text{sr}^{-1} \cdot \text{s}^{-1}$ (a ratio of ~ 1.9) with a similar order as the increase in solar wind dynamic
431 pressure.

432 Such increase can be explained, according to the simulation results by several mechanisms. The
433 increase of the dynamic pressure leads to a global increase of the energy and intensity of the ion
434 precipitating into the atmosphere. In terms of energy differential precipitating flux, this is equivalent
435 to a shift in energy of the flux proportional to the increase of the solar wind convective electric field
436 intensity upstream to Mars, and an increase of the intensity of the energy differential precipitating
437 flux, proportional to the increase of the solar wind flux because an increase of the solar wind flux also
438 implies a change of the charge exchange rate between the incident solar wind ions and the planetary
439 exosphere. Such effect is particularly observable above 1 keV in the simulated precipitating ion energy
440 flux where the flux is in a large proportion composed of planetary oxygen ions formed by charge
441 exchange.

442

443 **Acknowledgements**

444 This work was supported by the DIM ACAV and the ESA/ESTEC faculty. This work was also supported
445 by CNES “Système Solaire” program and by the “Programme National de Planétologie” and
446 “Programme National Soleil-Terre”. This work is also part of HELIOSARES Project supported by the ANR

447 (ANR-09-BLAN-0223), ANR MARMITE (ANR-13-BS05-0012-02) and ANR TEMPETE (ANR-17-CE31-0016).
448 Spacecraft data used in this paper are archived and available in the Planetary Data System Archive
449 (<https://pds.nasa.gov/>). Numerical simulation results used in this article can be found in the simulation
450 database (<http://impex.latmos.ipsl.fr>).

451

452

453 **References**

454 Acuña, M. H., et al. (1999), Global distribution of crustal magnetization discovered by the Mars Global
455 Surveyor MAG/ER Experiment, *Science*, 284, 790-793, doi:10.1126/science.284.5415.790.

456 Anderson D.E and C.W. Hord, Multidimensional radiative transfer: Applications to planetary coronae,
457 *Planetary and Space Science*, Volume 25, Issue 6, 1977, Pages 563-571, ISSN 0032-0633,
458 [https://doi.org/10.1016/0032-0633\(77\)90063-0](https://doi.org/10.1016/0032-0633(77)90063-0).

459 Andersson, L., R. E. Ergun, and A. I. F. Stewart (2010), The Combined Atmospheric Photochemistry and
460 Ion Tracing code: reproducing the Viking Lander results and initial outflow results, *Icarus*, 206(1), 120–
461 129, <https://doi.org/10.1016/j.icarus.2009.07.009>.

462 Barabash, S., Lundin, R., Andersson, H. et al. (2006), The analyzer of space plasmas and energetic atoms
463 (ASPERA-3) for the Mars Express mission, *Space. Sci. Rev.*, 126, 113-164,
464 <https://doi.org/10.1007/s11214-006-9124-8>

465 Brain, D. A., F. Bagenal, Y.-J. Ma, H. Nilsson, and G. Stenberg Wieser (2016), Atmospheric escape from
466 unmagnetized bodies, *J. Geophys. Res. Planets*, 121, 2364–2385, doi:[10.1002/2016JE005162](https://doi.org/10.1002/2016JE005162).

467 Chassefière, E., and F., Leblanc (2004), Mars atmospheric escape and evolution; interaction with the
468 solar wind, *Planet. Space Sci.*, 52, 1039-1058, doi: 10.1016/j.pss.2004.07.002

469 Chaufray, J. Y., R. Modolo, F. Leblanc, G. Chanteur, R. E. Johnson, and J. G. Luhmann (2007), Mars solar
470 wind interaction: Formation of the Martian corona and atmospheric loss to space, *J. Geophys. Res.*,
471 112, E09009, doi:10.1029/2007JE002915.

472 Chaufray, J.-Y., Gonzalez-Galindo, F., Forget, F., Lopez-Valverde, M., Leblanc, F., Modolo, R., Hess, S.,
473 Yagi, M., Blelly, P.-L., and Witasse, O. (2014), Three-dimensional Martian ionosphere model: II. Effect
474 of transport processes due to pressure gradients, *J. Geophys. Res. Planets*, 119, 1614– 1636,
475 doi:[10.1002/2013JE004551](https://doi.org/10.1002/2013JE004551).

476 Chicarro, A., P. Martin, and R. Trautner (2004), The Mars Express mission: An overview, in *Mars*
477 *Express: A European Mission to the Red Planet*, *Eur. Space Agency Spec. Publ., ESA SP-1240*, edited by
478 A. Wilson and A. Chicarro, pp. 3–16, ESA Publ. Div., ESTEC, Noordwijk, Netherlands.

479 Connerney, J.E.P., Espley, J., Lawton, P. et al., The MAVEN Magnetic Field Investigation, *Space Sci Rev*
480 (2015a) 195 : 257., <https://doi.org/10.1007/s11214-015-0169-4>

481 Connerney, J.E.P., Espley, J.R., DiBraccio, G.A., et. al. (2015b). First results of the MAVEN magnetic field
482 investigation. *Geophys. Res. Lett.*, 42, 8819–8827, doi:10.1002/2015GL065366.

483 Curry S. M., Luhmann J. G., and al. (2015), Response of Mars 0+ pickup ions to the 8 March 2015 ICME:
484 Inferences from MAVEN data-based models., *Geophys. Res. Lett.*, 42, 9095-9102,
485 doi:10.1002/2015GL06304.

486 Diéval, C., et al. (2012), A case study of proton precipitation at Mars: Mars Express observations and
487 hybrid simulations, *J. Geophys. Res.*, 117, A06222, doi:[10.1029/2012JA017537](https://doi.org/10.1029/2012JA017537).

488 Dong, Y., Fang, X., Brain, D. A., McFadden, J. P., Halekas, J. S., Connerney, J. E. P., Eparvier, F.,
489 Andersson, L., Mitchell, D., and Jakosky, B. M. (2017), Seasonal variability of Martian ion escape
490 through the plume and tail from MAVEN observations, *J. Geophys. Res. Space Physics*, 122, 4009–4022,
491 doi:10.1002/2016JA023517.

492 Edberg, N., Brain, D. A., Lester, M., Cowley, S. W. H., Modolo, R., Franz, M., and Barabash S. (2009),
493 « Plasmas boundary variability at Mars as observed by Mars Global Surveyor and Mars Express », *Ann.*
494 *Geophys.*, 27, 3537-3550, doi:10.5194/angeo-27-3537-2009.

495 Edberg, N. J. T., Lester, M., Cowley, S. W. H., Brain, D. A., Fränz, M., and Barabash, S. (2010),
496 Magnetosonic Mach number effect of the position of the bow shock at Mars in comparison to Venus,
497 *J. Geophys. Res.*, 115, A07203, doi:[10.1029/2009JA014998](https://doi.org/10.1029/2009JA014998).

498 Eparvier, F.G., Chamberlin, P.C., Woods, T.N. et al., The Solar Extreme Ultraviolet Monitor for MAVEN,
499 *Space Sci Rev* (2015) 195 : 293., <https://doi.org/10.1007/s11214-015-0195-2>

500 Fang, X., Liemohn, M. W., Nagy, A. F., Luhmann, J. G., and Ma, Y. (2010), Escape probability of Martian
501 atmospheric ions: Controlling effects of the electromagnetic fields, *J. Geophys. Res.*, 115, A04308,
502 doi:[10.1029/2009JA014929](https://doi.org/10.1029/2009JA014929).

503 Fang, X., S. W. Bougher, R. E. Johnson, J. G. Luhmann, Y. Ma, Y.-C. Wang, and M. W. Liemohn (2013),
504 The importance of pickup oxygen ion precipitation to the Mars upper atmosphere under extreme solar
505 wind conditions, *Geophys. Res. Lett.*, 40, 1922–1927, doi:10.1002/grl.50415.

506 Forget, F., Hourdin, F., Fournier, R., Hourdin, C., Talagrand, O., Collins, M., ... Huot, J.-P. (1999).
507 Improved general circulation models of the Martian atmosphere from the surface to above 80 km.
508 *Journal of Geophysical Research*, 104(E10), 24,155–24,175. <https://doi.org/10.1029/1999JE001025>

509 Fedorov A., Budnik E., Sauvaud J.-A., Mazelle C., Barabash S., Lundin R., Acuña M., Holmström M.,
510 Grigoriev A., Yamauchi A., Andersson H., Thocaven J.-J., Winningham D., Frahm R., Sharber J.R.,
511 Scherrer J., Coates A.J., Linder D.R., Kataria D.O., Kallio E., Koskinen H., Säles T., Riihelä P., Schmidt W.,
512 Kozyra J., Luhmann J., Roelof E., Williams D., Livi S., Curtis C.C., Hsieh K.C., Sandel B.R., Grande M.,
513 Carter M., McKenna-Lawler S., Orsini S., Cerulli-Irelli S., Maggi M., Wurz P., Bochsler P., Krupp N., Woch
514 J., Fränz M., Asamura K., Dierker C., Structure of the Martian wake, *Icarus*, Volume 182, Issue 2, 2006,
515 Pages 329-336, ISSN 0019-1035, <https://doi.org/10.1016/j.icarus.2005.09.021>.

516 Fox, J.. (2004). Response of the Martian thermosphere/ionosphere to enhanced fluxes of solar soft X
517 rays. *Journal of Geophysical Research*. 109. Doi:10.1029/2004JA010380.

518 Halekas, J.S., Taylor, E.R., Dalton, G. et al., The Solar Wind Ion Analyzer for MAVEN, *Space Sci Rev* (2015)
519 195 : 125., <https://doi.org/10.1007/s11214-013-0029-z>

520 Halekas, J. S., et al. (2017), Structure, dynamics, and seasonal variability of the Mars-solar wind
521 interaction: MAVEN Solar Wind Ion Analyzer in-flight performance and science results, *J. Geophys. Res.*
522 *Space Physics*, 122, 547–578, doi: 10.1002/2016JA023167.

523 Hall, B. E. S., et al. (2016), Annual variations in the Martian bow shock location as observed by the Mars
524 Express mission, *J. Geophys. Res. Space Physics*, 121, 11,474– 11,494, doi:[10.1002/2016JA023316](https://doi.org/10.1002/2016JA023316).

525 Hara, T., K. Seki, Y. Futaana, M. Yamauchi, M. Yagi, Y. Matsumoto, M. Tokumaru, A. Fedorov, and S.
526 Barabash (2011), Heavy-ion flux enhancement in the vicinity of the Martian Ionosphere during CIR
527 passage: Mars Express ASPERA-3 observations, *Journal of Geophysical Research*, vol. 116, A02309,
528 doi:10.1029/2010JA015778, 2011.

529 Hara, T., et al. (2017a), MAVEN observations on a hemispheric asymmetry of precipitating ions toward
530 the Martian upper atmosphere according to the upstream solar wind electric field, *J. Geophys. Res.*
531 *Space Physics*, 122, 1083–1101, doi: 10.1002/2016JA023348

532 Hara T. et al., (2017b), Evidence for crustal magnetic field control of ions precipitating into the upper
533 atmosphere of Mars, *J. Geophys. Res. Space Physics*, 122, doi: 10.1029/2017JA024798.

534 Jakosky, B.M., Lin, R.P., Grebowsky, J.M. et al., The Mars Atmosphere and Volatile Evolution (MAVEN)
535 Mission, *Space Sci Rev* (2015) 195 : 3. <https://doi.org/10.1007/s11214-015-0139-x>

536 Jarvinen, R., and Kallio, E. (2014), Energization of planetary pickup ions in the solar system, *J. Geophys.*
537 *Res. Planets*, 119, 219– 236, doi:[10.1002/2013JE004534](https://doi.org/10.1002/2013JE004534).

538 Jarvinen, R., Brain, D. A., Modolo, R., Fedorov, A., & Holmström, M. (2018). Oxygen ion energization at
539 Mars: Comparison of MAVEN and Mars express observations to global hybrid simulation. *Journal of*
540 *geophysical research: Space physics*, 123(2), 1678-1689. <https://doi.org/10.1002/2017JA024884>

541 Johnson, R.E., Plasma-induced sputtering of an atmosphere, *Space Sci Rev* (1994) 69: 215.
542 <https://doi.org/10.1007/BF02101697>

543 Johnson, R. E., D. Schnellenberger, and M. C. Wong (2000), The sputtering of an oxygen thermosphere
544 by energetic O⁺, *J. Geophys. Res.*, 105(E1), 1659–1670, doi:10.1029/1999JE001058.

545 Krasnopolsky, V. A., and P. D. Feldman (2001). Detection of molecular hydrogen in the atmosphere of
546 Mars. *Science*, 294,1914– 1917.

547 Leblanc, F. and R.E Johnson, Sputtering of the Martian atmosphere by solar wind pick-up ions, *Planet.*
548 *Space Sci.*, 49, 645-656, 2001, doi:10.1016/S0032-0633(01)00003-4.

549 Leblanc F. and R.E. Johnson (2002), Role of molecules in pick-up ion sputtering of the Martian
550 atmosphere, *J. Geophys. Res.*, <https://doi.org/10.1029/2000JE001473>

551 Leblanc F., R. Modolo and al. (2015), Mars heavy ion precipitating flux as measured by Mars
552 Atmosphere and Volatile Evolution, *Geophys. Res. Lett.*, 42, 9135-9141, doi: 10.1002/2015GL066170.

553 Leblanc, F., Chaufray, J. Y., Modolo, R., Leclercq, L., Curry, S., Luhmann, J., ... Jakosky, B. (2017). On the
554 origins of Mars' exospheric nonthermal oxygen component as observed by MAVEN and modeled by
555 HELIOSARES. *Journal of Geophysical Research: Planets*, 122, 2401–2428.
556 <https://doi.org/10.1002/2017JE005336>

557 Lillis, R.J., Brain, D.A., Bougher, S.W. et al., Characterizing Atmospheric Escape from Mars Today and
558 Through Time, with MAVEN, *Space Sci Rev* (2015) 195: 357. [https://doi.org/10.1007/s11214-015-0165-](https://doi.org/10.1007/s11214-015-0165-8)
559 [8](https://doi.org/10.1007/s11214-015-0165-8)

560 Lillis, R. J., et al. (2017), Photochemical escape of oxygen from Mars: First results from MAVEN in situ
561 data, *J. Geophys. Res. Space Physics*, 122, 3815– 3836, doi:[10.1002/2016JA023525](https://doi.org/10.1002/2016JA023525).

562 Luhmann, J. G. (1990), A model of the ion wake of Mars, *Geophysical Research Letters*, 17, 869– 872,
563 <https://doi.org/10.1029/GL017i006p00869>

564 Luhmann, J. G., and J. U. Kozyra (1991), Dayside pick-up oxygen ion precipitation at Venus and Mars:
565 Spatial distributions, energy deposition and consequences, *J. Geophys. Res.*, 96(A4), 5457–5467, doi:
566 10.1029/90JA01753.

567 Luhmann, J. G., R. E. Johnson, M. H. G. Zhang, Evolutionary impact of sputtering of the Martian
568 atmosphere by O⁺ pickup ions, *Geophys. Res. Lett.*, 19, 2151–2154, 1992.
569 <https://doi.org/10.1029/92GL02485>

570 Lundin, R., A. Zakharov, R. Pellinen, et al. (1990), ASPERA/ Phobos measurements of the ion outflow
571 from the Martian ionosphere, *Geophysical Research Letters*, 17, 873–876,
572 <https://doi.org/10.1029/GL017i006p00873>

573 Lundin, R., Barabash, S., Fedorov, A., Holmström, M., Nilsson, H., Sauvaud, J.-A., & Yamauchi, M.
574 (2008), Solar forcing and planetary ion escape from Mars, *Geophysical Research Letters*, 35, L09203,
575 doi: 10.1029/2007GL032884.

576 Martinez, A., Leblanc, F., Chaufray, J. Y., Modolo, R., Romanelli, N., Curry, S., et al (2019a). Variability
577 of precipitating ion fluxes during the September 2017 event at Mars. *Journal of Geophysical Research:*
578 *Space Physics*, 124. <https://doi.org/10.1029/2018JA026123>

579 Martinez, A., Leblanc, F., Chaufray, J. Y., Modolo, R., Witasse, O., Dong, Y., et al. (2019b). Influence of
580 extreme ultraviolet irradiance variations on the precipitating ion flux from MAVEN observations.
581 *Geophysical Research Letters*, 46. <https://doi.org/10.1029/2019GL083595>

582 Masunaga, K., et al. (2017), Statistical analysis of the reflection of incident O⁺ pickup ions at Mars:
583 MAVEN observations, *J. Geophys. Res. Space Physics*, 122, 4089–4101, doi:10.1002/2016JA023516.

584 Modolo R., G. M. Chanteur, E. Dubinin and A. P. Matthews (2005), Influence of the solar EUV flux on
585 the Martian plasma environment, *Ann. Geophys.*, 23, 433–444, doi:[10.5194/angeo-23-433-2005](https://doi.org/10.5194/angeo-23-433-2005).

586 Modolo, R., et al. (2016), Mars-solar wind interaction: LatHyS, an improved parallel 3-D multispecies
587 hybrid model, *J. Geophys. Res. Space Physics*, 121, 6378–6399, doi: 10.1002/2015JA022324.

588 Ramstad, R., S. Barabash, F. Yoshifumi, and M. Holmström (2017), Solar wind- and EUV-dependent
589 models for the shapes of the Martian plasma boundaries based on Mars Express measurements, *J.*
590 *Geophys. Res. Space Physics*, 122, 7279–7290, doi:[10.1002/2017JA024098](https://doi.org/10.1002/2017JA024098).

591 Rahmati, D. E. Larson, T. E. Cravens et al., MAVEN insights into oxygen pickup ions at Mars, *Geophysical*
592 *Research Letters*, 42, 21, (8870-8876), (2015). <https://doi.org/10.1002/2015GL065262>

593 Romanelli, N., Modolo, R., Leblanc, F., Chaufray, J.-Y., Martinez, A., Ma, Y., et al. (2018). Responses of
594 the Martian magnetosphere to an interplanetary coronal mass ejection: MAVEN observations and
595 LatHyS results. *Geophysical Research Letters*, 45, 7891– 7900. <https://doi.org/10.1029/2018GL077714>

596 Trotignon, J. G., Mazelle C., Bertucci C., and Acuna M. H. (2006), Martian shock and magnetic pile-up
597 boundary positions and shapes determined from the Phobos 2 and Mars Global Surveyor data sets,
598 *Planet. Space Sci.*, 54, 357-369, doi:10.1016/j.pss.2006.01.003.

599 Wang, Y.-C., J. G. Luhmann, F. Leblanc, X. Fang, R. E. Johnson, Y. Ma, W.-H. Ip, and L. Li (2014), Modeling
600 of the O⁺ pickup ion sputtering efficiency dependence on solar wind conditions for the Martian
601 atmosphere, *J. Geophys. Res. Planets*, 119, 93–108, doi: 10.1002/2013JE004413.

602 Wang, Y.-C., J. G. Luhmann, X. Fang, F. Leblanc, R. E. Johnson, Y. Ma, and W.-H. Ip (2015), Statistical
603 studies on Mars atmospheric sputtering by precipitating pickup O⁺: Preparation for the MAVEN
604 mission, *J. Geophys. Res. Planets*, 120, 34–50, doi: 10.1002/2014JE004660

605 Yagi, M., Leblanc, F., Chaufray, J. Y., Gonzalez-Galindo, F., Hess, S., & Modolo, R. (2012). Mars
606 exospheric thermal and non-thermal components: Seasonal and local variations. *Icarus*, 221(2), 682–
607 693. <https://doi.org/10.1016/j.icarus.2012.07.022>

Figure 1.

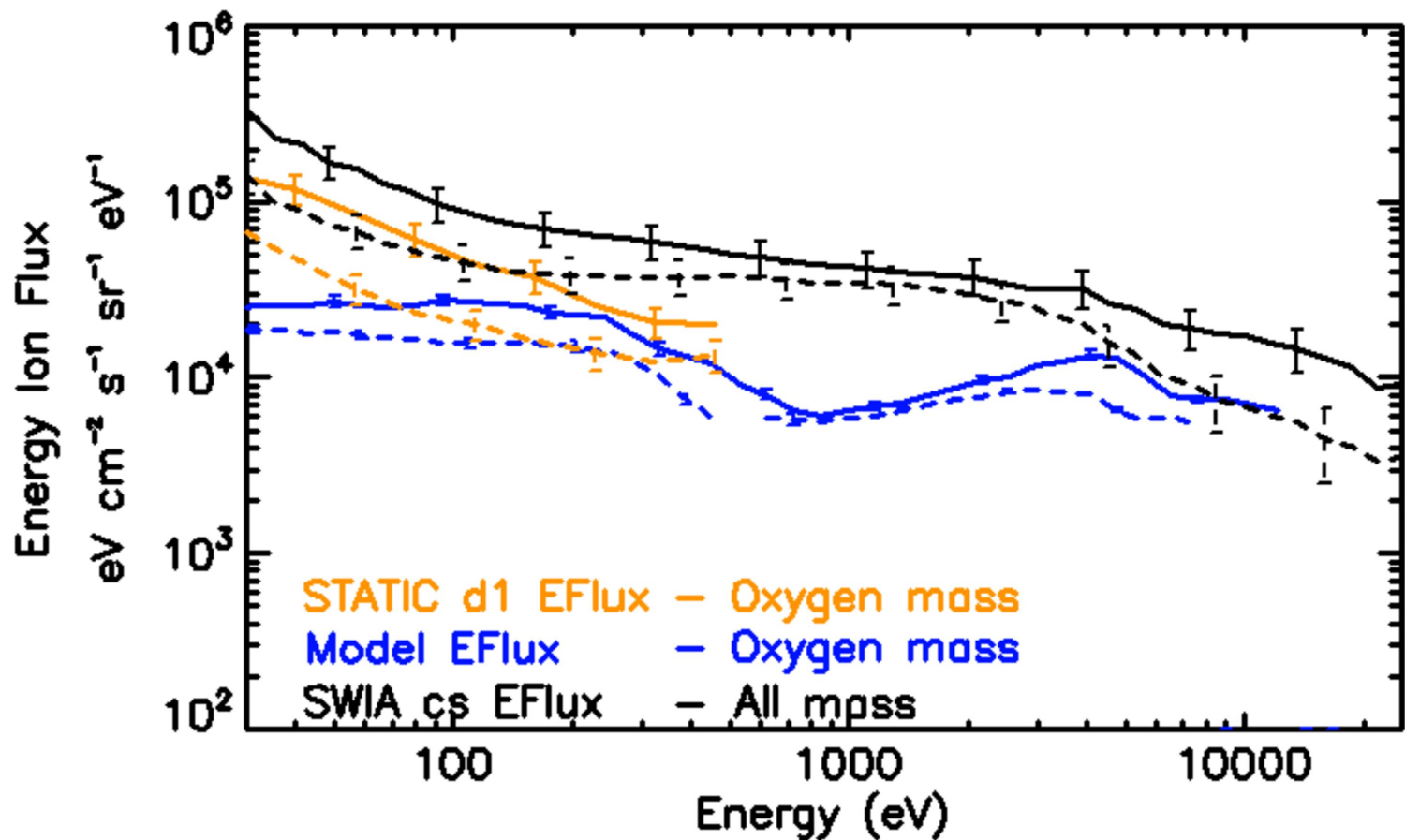


Figure 2.

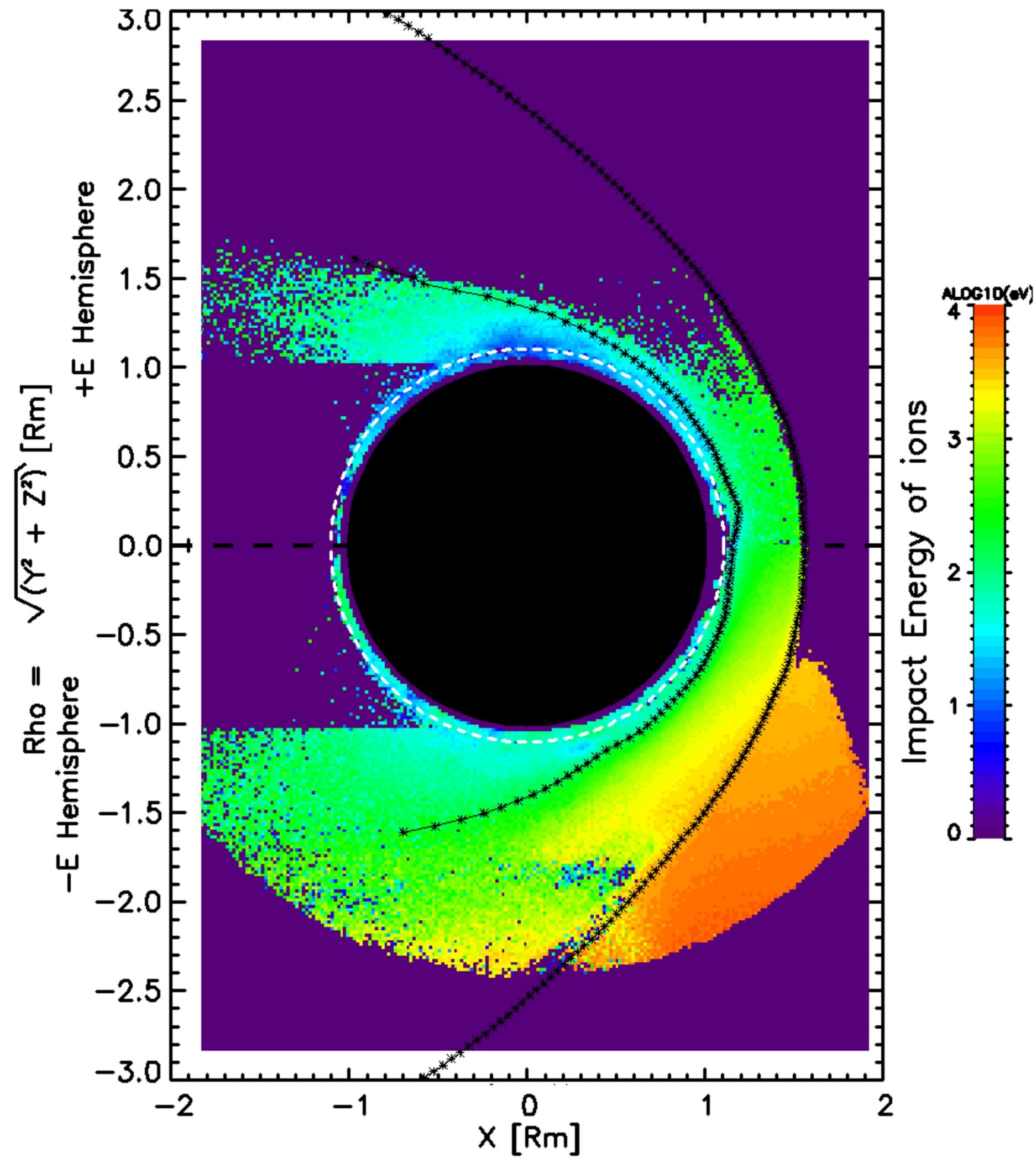


Figure 3.

